Inorganic Chemistry

pubs.acs.org/IC

Article

Study of the Temperature- and Pressure-Dependent Structural Properties of Alkali Hydrido-*closo*-borate Compounds

Romain Moury,* Zbigniew Łodziana,* Arndt Remhof, Léo Duchêne, Elsa Roedern, Angelina Gigante, and Hans Hagemann*

Cite This: *Inorg. Chem.* 2022, 61, 5224−5233

Read Online

ACCESS | Metrics & More | Article Recommendations | Supporting Information

ABSTRACT: In this work, we report on the structural properties of alkali hydrido-*closo*-(car)borates, a promising class of solid-state electrolyte materials, using high-pressure and temperature-dependent X-ray diffraction experiments combined with density functional theory (DFT) calculations. The mechanical properties are determined via pressure-dependent diffraction studies and DFT calculations; the shear moduli appear to be very low for all studied compounds, revealing their high malleability (that can be beneficial for the manufacturing and stable cycling of all-solid-state batteries). The thermodiffraction experiments also reveal a high coefficient of thermal expansion for these materials. We discover a pressure-induced phase transition for $K_2B_{12}H_{12}$ from $Fm\bar{3}$ to *Pnnm* symmetry around 2 GPa. A temperature-induced phase transition for $Li_2B_{10}H_{10}$ was also observed for the first time by thermodiffraction, and the crystal structure determined by combining experimental data and DFT calculations. Interestingly, all phases of the studied compounds (including newly discovered high-pressure and high-temperature phases) may be related via a group−subgroup relationship, with the notable exception of the room-temperature phase of $Li_2B_{10}H_{10}$.

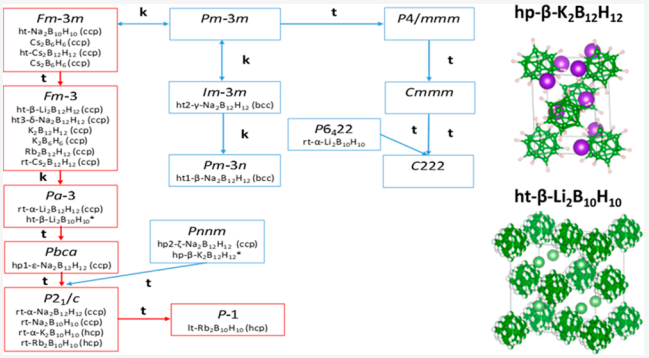

INTRODUCTION

Since the discovery of superionic conductivity in the high-temperature phase of $Na_2B_{12}H_{12}$,[1] there has been an increasing interest in hydrido-*closo*-(car)borates (H-*c*-B) and hydrido-*nido*-(car)borates and their solid solutions,[2−11] as well as their halogenated derivatives.[12] Several of these compounds or solid solutions exhibit very high ionic conductivities of >1 mS/cm at room temperature and are chemically and electrochemically very stable.[13,14] Recently, some prototypes of all-solid-state batteries using hydrido-*closo*-(car)borates as electrolytes have demonstrated very promising performances.[15,16] Furthermore, novel cost-effective methods have been developed to synthesize hydrido-*closo*-borates from solution,[17,18] allowing electrode impregnation to notably improve the ionic contact between the electrode and electrolyte.[19] These results demonstrate that this family presents many excellent properties as solid ionic conductors for new generations of all-solid-state batteries.

Understanding the bulk mechanical properties of solid electrolytes in general and H-*c*-B in particular is crucial for developing a manufacturing method for all-solid-state batteries as well as for improving their cycling stability.[20] For example, charging and discharging cycles can induce changes in the volume of the electrode materials, which should be accommodated by the solid electrolyte without mechanically disrupting the electrode−electrolyte interface. Some of the authors have demonstrated that a solid electrolyte based on a solid solution between H-*c*-B and hydrido-*closo*-carborate is stable for at least 800 charging/discharging cycles.[21] Mechanical properties such as the shear modulus of the solid electrolyte are also considered to be important parameters in some models of dendrite formation in solid electrolytes.[22] Thermal expansion of the materials constituting the battery may also induce mechanical stress when the battery is subject to overheating. A colossal barocaloric effect has also been predicted for $Li_2B_{12}H_{12}$;[23] hence, the behaviors of this family of materials with pressure and temperature are important aspects of understanding these properties. Furthermore, while the fundamental crystal chemistry of hydrido-*closo*-borates is well established,[24] some pieces are still missing. For instance, a temperature-induced phase transition has been observed by differential scanning calorimetry (DSC) experiments for $Li_2B_{10}H_{10}$ and $(K,Cs)_2B_{12}H_{12}$, though no crystal structure

Received: November 25, 2021
Published: March 24, 2022

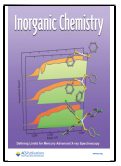

was given.[25,26] In addition, only a few reports about the high-pressure behavior for this family of compounds exist, except for $(Na,Cs)_2B_{12}H_{12}$.[27,28] In this context, insight into their structural behavior under external stimuli (pressure and temperature) is a critical aspect for extracting some fundamental knowledge and physical properties, as the coefficients of thermal expansion (CTEs) and the isothermal compressibility, of this class of compounds. In this work, we have investigated the temperature- and pressure-dependent X-ray diffraction of a series of H-*c*-B and $NaCB_{11}H_{12}$ to provide experimental data of the thermal expansion and compressibility of constituents of solid-state sodium and lithium ionic conductors. In our investigations, we have discovered and determined two new polymorphs, namely, high-temperature (ht, for temperatures above room temperature) β-$Li_2B_{10}H_{10}$ and high-pressure (hp) β-$K_2B_{10}H_{10}$. These experimental results are completed by theoretical density functional theory (DFT) calculations, and a comprehensive analysis of the structural and vibrationnal behavior of these materials is given.

BACKGROUND

Even though H-*c*-B exhibit a very rich crystal chemistry with numerous temperature- and pressure-induced phase transitions, they share most of the time common aristotypes such as cubic close packing (*ccp*), hexagonal close packing (*hcp*), and body center cubic (*bcc*) arrangements.[24] Along the series of alkali dodeca H-*c*-B, at ambient pressure and temperature, the larger cations $(K,Rb,Cs)_2B_{12}H_{12}$ crystallize in the cubic $Fm\bar{3}$ space group and $Li_2B_{12}H_{12}$ crystallizes in the cubic $Pa\bar{3}$ space group with undistorted *ccp* while $Na_2B_{12}H_{12}$ adopts monoclinic $P2_1/c$ symmetry with the distorted *ccp*. With respect to the deca H-*c*-B, $(Na,K,Rb)_2B_{10}H_{10}$ adopt the monoclinic $P2_1/c$ space group with distorted *ccp*, *hcp*, and *hcp*, respectively, whereas $Li_2B_{10}H_{10}$ stands as an exception with hexagonal space group $P6_422$ without cubic or hexagonal compact underlying packing. Their temperature-induced polymorphic phase transitions have been studied and determined for $(Li,Na,Rb,Cs)_2B_{12}H_{12}$ and $Na_2B_{10}H_{10}$,[26,29,30] while pressure-induced phase transitions have been investigated solely for $Na_2B_{12}H_{12}$. It undergoes two-phase transitions at relatively low pressures: $P2_1/c \rightarrow$ [0.3−0.8 GPa] $Pbca \rightarrow$ [5.7−8.1 GPa] *Pnnm*.[27] Figure 1 shows the different symmetries encountered for all of the known H-*c*-B together with their underlying packing in a group−subgroup graph. It is worth noting that most of the H-*c*-B exhibit a direct group−subgroup relationship (red path in Figure 1) that can come into play for the phase transitions for these compounds as discussed in detail for the pressure-induced transitions of $Na_2B_{12}H_{12}$.[27] Furthermore, the preferred packing for this family is *ccp* with the exception of ht polymorphs of $Na_2B_{12}H_{12}$ adopting the *bcc* packing for ht1-β-$Na_2B_{12}H_{12}$ and ht2-γ-$Na_2B_{12}H_{12}$. $Na_2B_{12}H_{12}$ possesses the richest phase diagram among all of the H-*c*-B, and it is the only one found in the *bcc* arrangement that is known to favor ionic conductivity.[31]

RESULTS AND DISCUSSION

Pressure Dependence. *High-Pressure X-ray Diffraction.* Six different samples [$(Li,Na,K)_2B_{12}H_{12}$, $(Li,K)_2B_{10}H_{10}$, and $NaCB_{11}H_{12}$] were investigated at Swiss Norwegian Beamline (SNBL) to study their behavior under pressure. Except for $Na_2B_{12}H_{12}$, for which the hp phase transitions were already described,[27] $K_2B_{12}H_{12}$ also undergoes a reversible phase

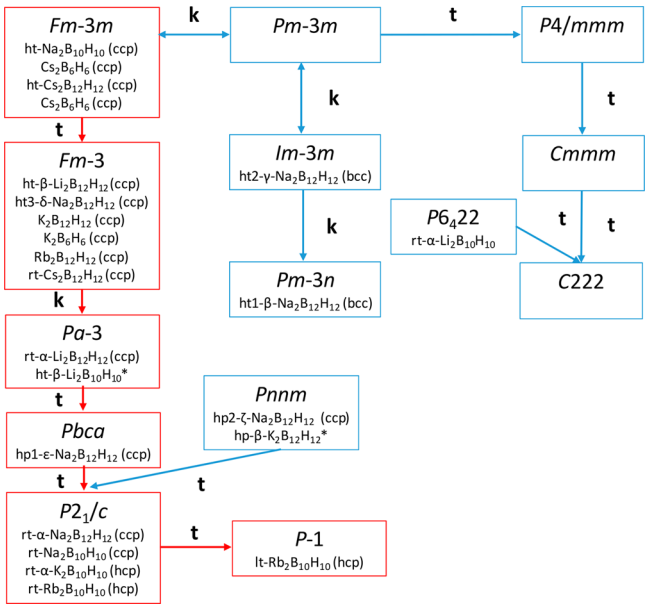

Figure 1. Group−subgroup relationship between the hydrido-*closo*-borates. **t** stands for the *translationengleich* subgroup, and **k** for the *klassengleich* subgroup. The asterisk indicates the crystal structures determined in this work. rt and lt stand for room temperature and low temperature (here below 250 K), respectively.

transition at >2 GPa toward a polymorph isostructural to hp2-ζ-$Na_2B_{12}H_{12}$ with orthorhombic *Pnnm* symmetry (Figure 2a). The cell parameters were first determined using Pawley refinement with hp2-ζ-$Na_2B_{12}H_{12}$ as first input and manually increased to fit the diffraction pattern; once a good approximation was found, the refinement was carried out. The Rietveld refinement was subsequently achieved with the as-obtained cell parameters and hp2-ζ-$Na_2B_{12}H_{12}$ atomic positions that enabled us to obtain hp-β-$K_2B_{12}H_{12}$ with the following cell parameters: a = 7.1670(13) Å, b = 9.212(6) Å, and c = 7.560(3) Å (Figure 2b). Despite the low quality of the pattern, due to the strains and preferential orientations induced by the pressure, refinement successfully converged with the following reliability factors: R_{wp} = 1.88, R_p = 1.16, and goodness of fit (GoF) = 6.5 (Figure S1).

Owing to the low quality of the diffraction pattern, DFT calculations were performed to further confirm the stability of the *Pnnm* symmetry. The diffraction peak at 8.2° cannot be explained by the refinement, which can be due to the remaining 111 reflection from the lp phase or another polymorph. The calculated pressure dependence of the free energy ($F = E_0 + pV$) reveals the phase transition of $K_2B_{12}H_{12}$ ($Fm\bar{3} \rightarrow Pnnm$) at 3.58 GPa, hence further confirming the experimental data (Figure S2). The phase transition is accompanied by an ∼7% specific volume change indicating a first-order transition. While a group−subgroup relationship exists between $Fm\bar{3}$ and *Pnnm*, a direct comparison of both structures does not allow identification of the transition mechanism. A transformation of the hp-β-$K_2B_{12}H_{12}$ *Pnnm* phase into $P2_1/c$, with $P2_1/c \subset Fm\bar{3}$, using matrices $\mathbf{a}_{mono} = -\mathbf{b}_{ortho} - \mathbf{c}_{ortho}$, $\mathbf{b}_{mono} = \mathbf{a}_{ortho}$, and $\mathbf{b}_{mono} = -\mathbf{b}_{ortho} + \mathbf{c}_{ortho}$ with an origin shift $\mathbf{c}_{mono} = \mathbf{c}_{ortho} + {}^1/_2$ (Figure S3) was performed prior to the comparison. The phase transition is diplacive combining a diffusionless (martensitic-like) transformation for the $B_{12}H_{12}^{2-}$ units with the displacement of the potassium cation like $Na_2B_{12}H_{12}$.[27] The martensitic-like transition is

https://doi.org/10.1021/acs.inorgchem.1c03681
Inorg. Chem. 2022, 61, 5224−5233

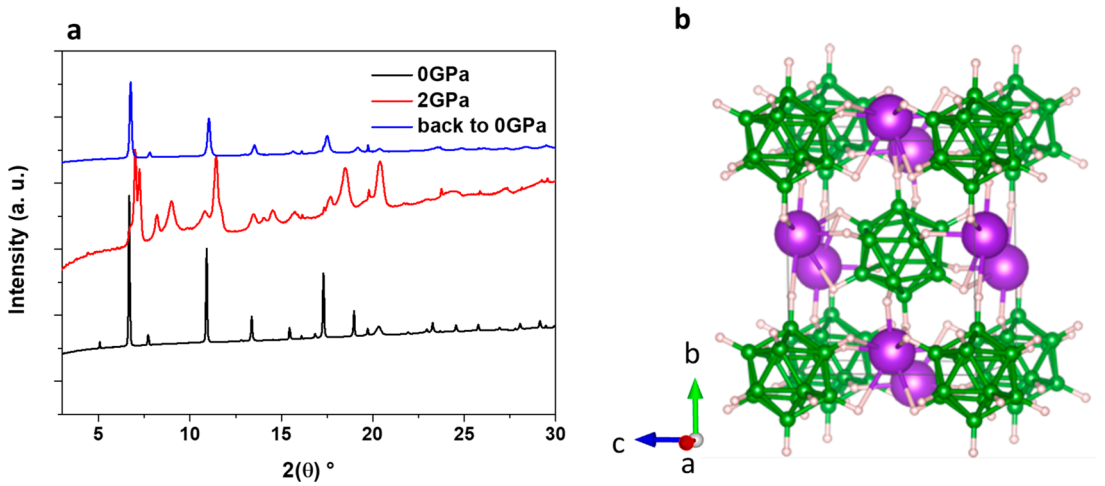

Figure 2. (a) Diffraction patterns of $K_2B_{12}H_{12}$ at 0 GPa (black), 2 GPa (red), and back to ambient pressure (blue) depicting the reversible pressure-induced phase transition. (b) Representation of the hp-β-$K_2B_{12}H_{12}$ crystal structure.

displayed in Figure S4, during which the cubic lattice is transformed into the monoclinic one. The deformation leads to the following high values of the Lagrangian strain tensor with $e_{11} = e_{33} = 0.1515$, $e_{22} = -0.2643$, and $e_{31} = e_{13} = 0.1272$, which must be taken into account to treat the phase transition using a finite strain approach. As a consequence, the Landau free energy must be built with an order parameter−strain coupling.[32] Using group theory analysis with amplimode,[33,34] on the Bilbao Crystallographic Server, one can identify that the decrease in symmetry from $Fm\bar{3}$ to $P2_1/c$ is driven by three one-dimensional irreducible representations (irreps) Γ^{4+} at wave vector k (0, 0, 0), X^+, and X^{2+} and one three-dimensional X^{2+} irrep at k (0, 1, 0).

Mechanical Properties. In the pressure range of 0−6 GPa, $Li_2B_{12}H_{12}$, $(Li,K)_2B_{10}H_{10}$, and $NaCB_{11}H_{12}$ do not undergo a pressure-induced phase transition. Together with those of hp2-ε-$Na_2B_{12}H_{12}$ and hp-β-$K_2B_{12}H_{12}$, their cell volumes were determined as a function of pressure. When the data allowed, experimental bulk moduli were determined by fitting the Murnaghan equation of state (eq 1) with the experimental data (Figure S5), and the results are listed in Table 1.

$$V(P) = V_0\left(1 + K_0'\frac{P}{K_0}\right)^{-1/B_0'} \quad (1)$$

The experimental bulk moduli determined for the compounds mentioned above are in the range of 16.3−25.5 GPa, revealing very high compressibility in good agreement with our previous study of $Na_2B_{12}H_{12}$.[27]

The elastic properties of the ordered phases of alkali H-*c*-B were also determined by DFT calculations (Table 1). They are in good agreement with experimental values, validating our calculation strategy. One has to keep in mind that calculated values correspond to the adiabatic constants while experimental data are for isothermal values. The evolution of the bulk (K) and shear (G) moduli as a function of the volume per formula unit is represented in Figure 3. For the Li cation, the bulk and shear moduli are systematically larger than for other elements of the group. Along the series $M_2B_{10}H_{10}$, the bulk modulus somewhat decreases for heavier cations, while for the $M_2B_{12}H_{12}$ family, one can observe a slight increase with the mass of the cation. The shear modulus does not follow any obvious trend; however, it is significantly smaller than for

Table 1. Summary of the Bulk (K) and Shear (G) Moduli Obtained Experimentally and by DFT of the Alkali Deca and Dodeca H-*c*-B[a]

compound	space group	G_r (GPa)	G_v (GPa)	K_r (GPa)	K_v (GPa)	K_{exp}
$Li_2B_{10}H_{10}$	$P6_422$ (No. 181)	6.20	7.43	20.01	20.46	16.3(4.6)
$Li_2B_{12}H_{12}$	$Pa\bar{3}$ (No. 205)	11.31	8.96	20.84	20.84	21.3(1.4)
$Na_2B_{10}H_{10}$	$P2_1/c$ (No. 14)	8.35	7.21	19.08	19.24	–
$Na_2B_{12}H_{12}$	$P2_1/c$ (No. 14)	2.11	6.08	7.20	16.10	13.1(6)
$K_2B_{10}H_{10}$	$P2_1/c$ (No. 14)	8.38	7.24	19.07	19.21	25.5(2.5)
$K_2B_{12}H_{12}$	$Fm\bar{3}$ (No. 202)	7.41	5.99	16.85	16.49	–
$Rb_2B_{10}H_{10}$	$P2_1/c$ (No. 14)	5.25	4.45	17.10	17.56	–
$Rb_2B_{12}H_{12}$	$Fm\bar{3}$ (No. 202)	7.34	5.94	16.80	16.80	–
$Cs_2B_{10}H_{10}$	$P2_1/c$ (No. 14)	2.33	3.14	10.25	15.27	–
$Cs_2B_{12}H_{12}$	$Fm\bar{3}$ (No. 202)	6.17	4.91	14.68	14.68	–

[a]The indices r and v stand for the Reuss and Voigt limits, respectively.

oxides or sulfides (>10 GPa).[35] This is an indication of the malleability of these compounds, especially with dodeca H-*c*-B anions; for example, following the Pugh criterion for ductile materials affords a K/G ratio of >1.75.[36]

The relatively large compressibility and malleability of H-*c*-B are beneficial for solid-state battery manufacturing, making it easier to densify the solid electrolyte layer and to achieve intimate contact with the electrode. If a good contact between the H-*c*-B and active material is established (via solution processing, for example),[19] it can be maintained upon cycling because of their high deformability. It is worth mentioning that mechanical properties obtained from structural studies cannot always be translated to bulk properties in a battery where a solid electrolyte is typically a pressed polycrystalline powder. Nevertheless, H-*c*-B have proven to maintain stable interfaces in all-solid-state batteries after many cycles, including without the application of significant external mechanical pressure.[21] The experimental and theoretical values appear to be

https://doi.org/10.1021/acs.inorgchem.1c03681
Inorg. Chem. 2022, 61, 5224−5233

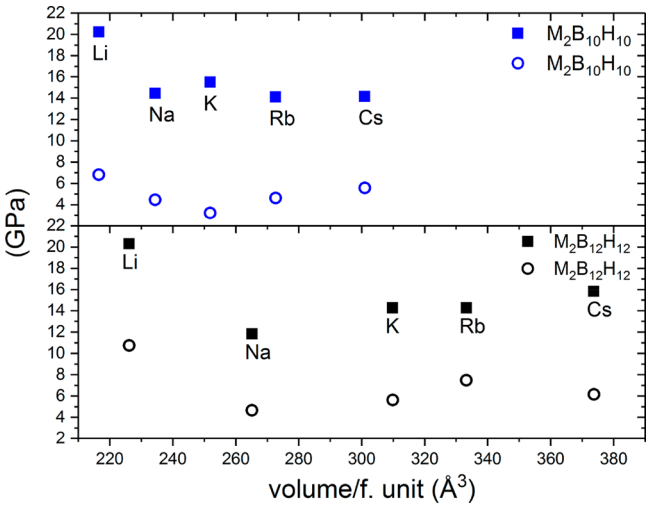

Figure 3. Calculated bulk (squares) and shear (circles) moduli for alkali metal deca and dodeca H-*c*-B. The average $(X_r + X_v)/2$ values are presented.

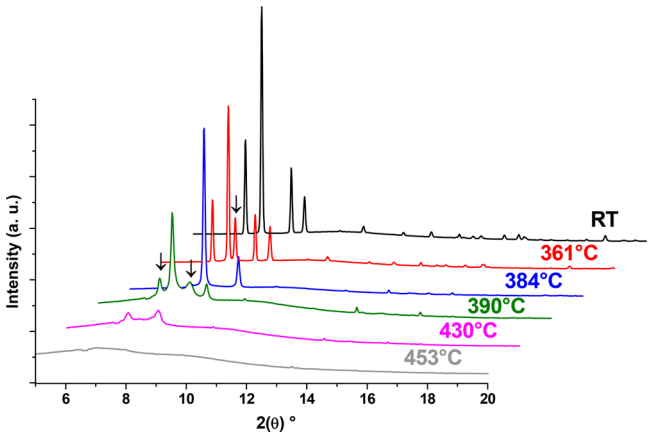

Figure 4. Temperature dependence of the diffraction patterns for $Li_2B_{10}H_{10}$. At room temperature, only rt-α-$LiB_{10}H_{10}$ is present. At 361 °C, ht-β-$LiB_{10}H_{10}$ appears (arrow), and both polymorphs coexist up to 384 °C. At 390 °C, the unidentified phase appears (arrow), and both phases coexist up to 430 °C. At 453 °C, amorphization of the material occurs.

characteristic for the entire series of compounds and can thus be extrapolated to predict the behavior of new ionic conductors based on H-*c*-B and derived compounds. Additionally, the very low shear modulus is an indication that such materials easily adapt to the structural changes of the electrode.

Temperature Dependence. *High-Temperature X-ray Diffraction.* Most of the crystal structures of deca and dodeca H-*c*-B of alkali metals are known for their low- and high-temperature polymorphs,[24,26,30] with the exceptions being the high-temperature phases of $Li_2B_{10}H_{10}$ and $(K,Rb)_2B_{12}H_{12}$, which were observed by DSC measurements, but the structure has never been determined.[25,26] $K_2B_{12}H_{12}$ undergoes a phase transition at ∼540 °C, which is around the transformation temperature of the glass capillary; hence, the transition was not recorded during our experiment. Nonetheless, we did observe a phase transition for rt-α-$Li_2B_{10}H_{10}$ starting to transform into ht-β-$Li_2B_{10}H_{10}$ at 361 °C. From this temperature, both polymorphs coexist up to 384 °C, at which rt-α-$LiB_{10}H_{10}$ totally transforms into ht-β-$LiB_{10}H_{10}$. At 390 °C, the diffraction peaks of ht-β-$LiB_{10}H_{10}$ start to decrease with the appearance of an amorphous and a new, crystal phase. The possible nature of this new crystal structure will be discussed below. From 430 °C, only the new and amorphous phases are present up to 453 °C, the temperature at which the compound becomes amorphous. Figure 4 displays the diffraction patterns for the different steps described. These observations are in good agreement with the previous study of the thermal behavior of $Li_2B_{10}H_{10}$, in which an entropically driven order−disorder phase transition was suggested.[25] However, the appearance of the unidentified crystal phase was never reported; due to the low quality of the diffraction pattern, a direct structural determination was not possible during our experiments, but the structure was likely determined with the support of DFT calculations (see below).

With regard to ht-β-$Li_2B_{10}H_{10}$, the phase appears to be isostructural to $Li_2B_{12}H_{12}$, and its pattern can be indexed with a cubic lattice with a = 9.5316(3) Å and V = 865.96(7) Å^3. The structure can be refined in two different space groups, $Fm\bar{3}m$ and $Pa\bar{3}$, with similar agreement factors (R_{wp} = 4.2 and 4.0 for $Pa\bar{3}$ and $Fm\bar{3}m$, respectively). In both structures, the $B_{10}H_{10}^{2-}$ ions are orientationally disordered as suggested in the previous study.[25]

DFT Calculations for ht-β-$Li_2B_{10}H_{10}$. These structures differ in the average orientation of $B_{10}H_{10}^{2-}$ anions, as shown in Figure S6. For the structure with $Pa\bar{3}$ symmetry, the $B_{10}H_{10}^{2-}$ anions are oriented such that the longer anion axis is along one of the principal lattice directions (three preferred orientations). This results in an average quasi-octahedral shape. For $Fm\bar{3}m$ symmetry, there are four orientations along the cubic unit cell diagonals preferred by $B_{10}H_{10}^{2-}$ anions. They average to the effective cubic shape of the anion (see Figure S6). Because both geometrical figures, the cube and the octahedron, have the same number of symmetry elements, the distinction between the two crystal structures of $Li_2B_{10}H_{10}$ must be related to the positions of cations, which is coupled to the anion orientation. To determine which of the two orientations are preferred (higher cohesive energy), we performed series of DFT calculations. Because the high-temperature phase is disordered, the procedure for the calculations was developed. The structures with random anion orientations/cation distribution were used to calculate the energy; the details are presented in the Supporting Information. The energy distribution for the atomic configurations in the cubic phase of $Li_2B_{10}H_{10}$ is presented in Figure 5. It consists of separated energy maxima starting with a ΔE of 0.014 eV/atom above the $P6_422$ ground-state energy up to a ΔE of 0.035 eV/atom for the least stable configurations. For four selected regions, the radial distribution functions (rdfs) for Li−H separation were calculated, as shown in the insets of Figure 5. In general, the rdf for the most stable configurations resembles that of the low-temperature phase, where two Li−H distances of 2.1 and 2.3 Å are present (they are larger than the values of 2.028, 2.044, and 2.216 Å reported for the experimental structure of $Li_2B_{10}D_{10}$).[25] For the least stable configurations, the Li−H separation strongly differs from the low-temperature one. The Li−H spacing has a broad distribution within the range of 1.9−2.7 Å. Such short interatomic distances indicate that Li is closely connected to anions. This can be seen in Figure 5 where the distribution of cations is shown for the structure with the lowest energy, and cations were confined to the tetrahedral interstitial voids. The cations with the least stable

https://doi.org/10.1021/acs.inorgchem.1c03681
Inorg. Chem. 2022, 61, 5224−5233

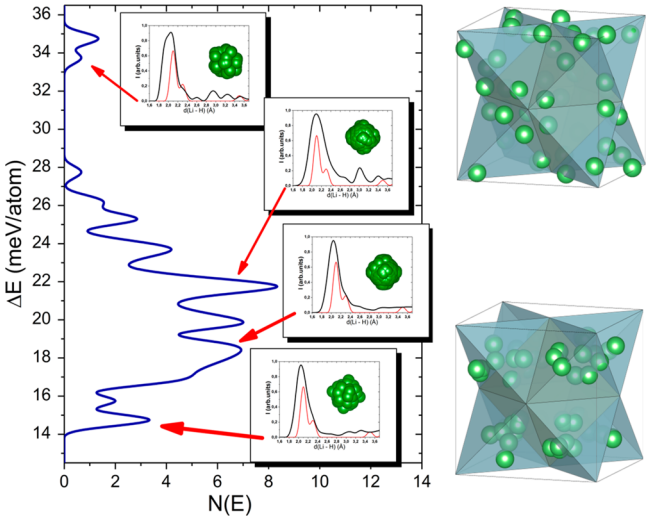

Figure 5. Energy distribution of $Li_2H_{10}H_{10}$ in the cubic *ccp* structure with respect to the *hcp* ($P6_422$) ground state. The insets show radial distribution functions for the Li−H separation; the red line is for the reference hexagonal structure. The green spheres are projections of anions on the (*a, b*) plane for the given energy range. The right side shows the distribution of cations corresponding to the configurations with the lowest and highest energies; for the sake of simplicity, only coordination tetrahedra of the *fcc* lattice are colored light blue.

configuration are located at tetrahedral facets rather than in the tetrahedral center. The projection of $B_{10}H_{10}^{2-}$ anion orientations on the (*a, b*) crystal plane indicates they are oriented with a longer axis along the (100), (010), or (001) lattice direction except for the least stable structure, where the orientation is along the unit cell diagonals (see Figure 5). This points toward $Pa\bar{3}$ space group symmetry for the high-temperature phase of $Li_2B_{10}H_{10}$ and a possible second phase transition to the $Fm\bar{3}m$ space group at higher temperatures prior to the thermal decomposition of the compound. Having this in mind, one can suggest that the unidentified ht phase could be the cubic $Fm\bar{3}m$ phase. A Rietveld refinement was then performed with an *a* of 10.219(3) Å; however, owing to the poor quality of the diffraction pattern, the fit was not optimal, but the solution cannot be excluded. Additional work would be necessary to demonstrate this last transition.

Coefficient of Thermal Expansion. CTEs were determined for several alkali hydrido-*closo*-(car)borates studied here by fitting the evolution of the volume as a function of the temperature to a polynomial function (eq 2). The CTE α can be determined using eq 3. The results are listed in Table 2.

$$V\ (\text{Å}^3) = V_0 + AT + BT^2 + CT^3 \tag{2}$$

$$\alpha\ (\text{K}^{-1}) = \frac{1}{V}\left(\frac{\partial V}{\partial T}\right)_p = \alpha_0 + DT + ET^2 \tag{3}$$

The relatively high value of the CTE, compared to those of oxides that are usually 2 orders of magnitude lower than the values of this family of compounds, points out a strong dilatation for these materials with temperature. This feature could induce mechanical stresses between the different components of the battery cathode (usually oxide-based), anode, and electrolyte. These mechanical stresses would be detrimental in the case of overheating. However, the very low shear moduli for these compounds could overcome this issue; the material will flow and with proper construction hence shall

Table 2. Summary of the Coefficients (V_0, *A*, *B*, and *C*) of the Polynomials Used to Fit the Evolution of the Volume of the Cells as a Function of Temperature Together with the Coefficients (α_0, *D*, and *E*) of the Equations of the CTE as a Function of Temperature and the Averages of the CTE [α(avg)] Calculated for the Indicated Temperature Range

compound	space group	V_0 (Å^3)	*A*	*B*	*C*	α(avg) (K^{-1})	α_0 (K^{-1})	*D* (K^{-2})	*E* (K^{-3})	*T* (K)
$Li_2B_{10}H_{10}$	$P6_422$	600.9(3)	0.020(1)	$3.9(1) \times 10^{-5}$	–	0.95×10^{-4}	$3.333(3) \times 10^{-5}$	$1.342(1) \times 10^{-7}$	$-1.67(1) \times 10^{-11}$	320–620
$Na_2B_{10}H_{10}$	$P2_1/c$	870.8(3)	0.123(1)	–	–	1.35×10^{-4}	$1.410(1) \times 10^{-4}$	–	–	300–380
$Na_2B_{10}H_{10}$	$Fm\bar{3}m$	891.2(4)	0.1376(7)	–	–	1.4×10^{-4}	$1.533(7) \times 10^{-4}$	–	–	400–795
$Na_4(B_{10}H_{10})(B_{12}H_{12})$	$Fm\bar{3}m$	900.5(6)	0.468(3)	$-5.50(7) \times 10^{-4}$	$3.19(4) \times 10^{-7}$	1.8×10^{-4}	$4.69(1) \times 10^{-4}$	$-1.098(3) \times 10^{-6}$	$9.32(2) \times 10^{-10}$	300–796
$K_2B_{12}H_{12}$	$Fm\bar{3}$	1141(1)	0.1838(2)	–	–	1.4×10^{-4}	$1.90(3) \times 10^{-5}$	–	–	305–724
$NaCB_9H_{10}$	$Pna2_1$	406.1(2)	0.1129(4)	–	–	2.5×10^{-4}	$2.751(1) \times 10^{-4}$	–	–	325–500
$Na_2B_{12}H_{12}$	$P2_1/c$	492	0.19	-3.8×10^{-4}	3.67×10^{-7}	1.3×10^{-4}	3.902×10^{-4}	7.723×10^{-7}	7.459×10^{-10}	273–540
$Na_2B_{12}H_{12}$	$Pm\bar{3}n$	457.9	0.12	–	–	2.3×10^{-4}	2.621×10^{-4}	–	–	540–580
$Na_2B_{12}H_{12}$	$Im\bar{3}m$	471.4	0.24	–	–	1.8×10^{-4}	5.091×10^{-4}	–	–	580–700
$Na_2B_{12}H_{12}$	$Fm\bar{3}m$	1051.1	0.14	-1.88×10^{-5}	–	1.1×10^{-4}	$1.109(1) \times 10^{-4}$	$-1.075(6) \times 10^{-11}$	–	540–750

https://doi.org/10.1021/acs.inorgchem.1c03681
Inorg. Chem. 2022, 61, 5224−5233

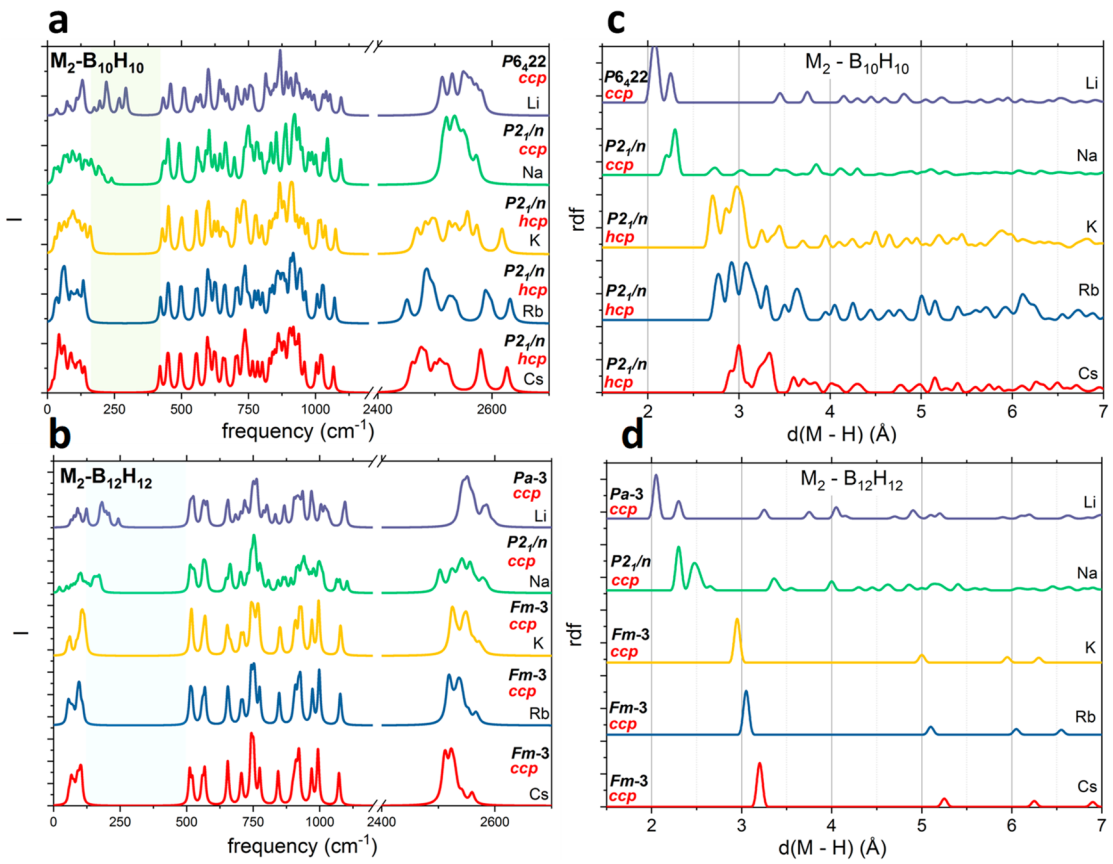

Figure 6. Distribution of the phonons at the Γ point for alkali metal (a) deca H-*c*-B and (b) dodeca H-*c*-B and the radial distribution function for cation−hydrogen separation for alkali metal (c) deca H-*c*-B and (d) dodeca H-*c*-B. The calculated frequencies are broadened with a 5 cm^{-1} Lorentzian.

not affect the interface. Low shear moduli can be seen as the behavior of the materials, with external stimuli, approaching that of the liquid. Additionally, elastic constants (Table 1) indicate the malleability of this class of materials. The thermal expansion is a manifestation of the anharmonicity of the lattice vibrations, and fitting the evolution of the volume as a function of the temperature with a polynomial on the order of ≥2 indicates a strong anharmonicity, related to the orientational disorder of anions.

Structural and Vibrational Analysis. Symmetry analysis reveals relations between space group symmetry of all alkali metal deca and dodeca H-*c*-B. The low-temperature hexagonal phase of $Li_2B_{10}H_{10}$ is somehow an exception from the family of structures originating from the $Pm\bar{3}m$ space group.

To improve our understanding of the similarities among members of this family of compounds, below we report on structural and vibrational analysis. In Figure 6, the distribution of the brillouin zone center modes for alkali metal deca and dodeca H-*c*-B together with the radial distribution function for metal−hydrogen separation is displayed. With regard to deca H-*c*-B, a clear division into two groups is apparent. Li and Na show a short separation between hydrogen and metal that can be correlated with the broader extent of the lattice modes. Especially for lithium, the lattice modes go beyond 250 cm^{-1}, which is an indication of direct and strong Li−$B_{10}H_{10}^{2-}$ interaction. More detailed information about internal $B_{10}H_{10}^{2-}$ vibrations can be found elsewhere;[37,38] however, the splitting of B−H modes (>2400 cm^{-1}) is related to the bond distortion, and the internal *closo*−cage vibrations in the range of 400−1200 cm^{-1} are modified by small deformations of the anion. The largest splitting of the highest-frequency modes (B−H stretching modes) is observed for the heaviest cations, K, Rb, and Cs. This is related to the *hcp* packing of anions,[24] rather than the *ccp* packing that is observed for Li and Na, and the symmetry of the $B_{10}H_{10}^{2-}$ molecule. This anion has point group symmetry *D*4*d* as for the capped square antiprism (see Figure 7). The distribution of cations is compatible with C_4 and S_8 symmetry elements of the molecule; thus, the differences can be ascribed to the packing of anions.

For these modes, similarities for K, Rb, and Cs are visible, which would be expected as these compounds have the same symmetry for the same anions. A large splitting of B−H modes for K, Rb, and Cs deca H-*c*-B should be noticed; they are related to the distribution of these cations in the lattice. For compounds with Li and Na, B−H stretches have distinct splittings of frequencies.[38] While the spectra related to the internal vibrations of anions have similarities within each class of compounds, the differences are related to the different site symmetry of the anion in Li- and Na-containing compounds. The largest differences between them are present in the upper range of lattice modes above 150 cm^{-1}. While for K, Rb, and Cs a clear gap between the lattice and internal anion modes is present, this gap is smaller for Li and Na, especially for $Li_2B_{10}H_{10}$, where lattice vibrations are present above 250 cm^{-1}; for Na, they are less extended, and for the icosahedral dodeca anion, they extend to lower frequencies.

In panels c and d of Figure 6, the pair distribution function calculated for metal−hydrogen separation is presented. For

https://doi.org/10.1021/acs.inorgchem.1c03681
Inorg. Chem. 2022, 61, 5224−5233

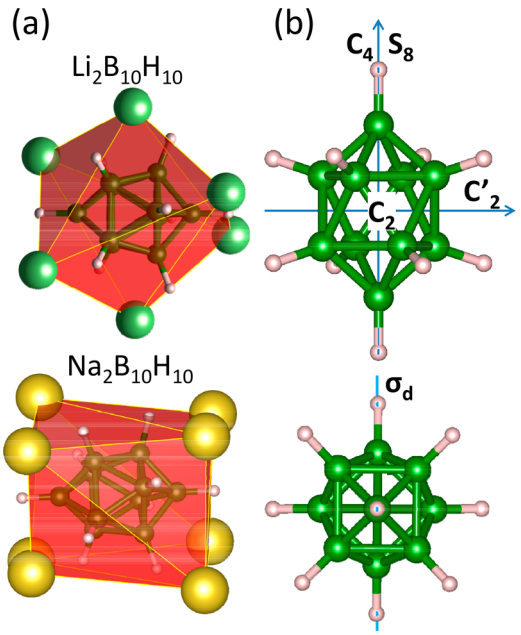

Figure 7. (a) Coordination polyhedra for $B_{10}H_{10}^{2-}$ anions in alkali metal deca H-*c*-B. Small green and gray spheres represent boron and hydrogen, respectively; large green spheres represent Li, and large yellow spheres Na. (b) Schematic view of the symmetry elements of the *D*4*d* point group of the $B_{10}H_{10}^{2-}$ anion. C_4 and S_8 are rotations/improper rotations around the 4- and 8-fold axes, respectively. C_2 and C'_2 are rotations around the 2-fold axis, and σ_d stands for the mirror plane.

both classes of compounds, clear differences are visible between Li/Na and heavier metals. While a well-defined Li−H separation of just >2 Å is visible for $Li_2B_{10}H_{10}$, these separations are still present in $Na_2B_{10}H_{10}$ with some additional peaks below 3 Å. All heavier alkali metals are separated from the nearest hydrogen by >2.5 Å, and the distribution of M−H distances is not well-defined for deca H-*c*-B (Figure 6c), showing a bond length distribution between 2.5 and 6 Å. The opposite is observed in dodeca H-*c*-B as the M−H spacing is well-defined for Cs, Rb, and K and decreases with the decrease in mass (radius) of the metal cation (Figure 6d). For Li and Na in dodeca H-*c*-B, this spacing is smaller (∼2 Å) and the distance distribution similar to that in deca H-*c*-B is clear, also for sodium.

The short metal−hydrogen distances for the two lightest metals are correlated with a broader range of their lattice modes and indicate direct M−H interaction. This is most apparent for $Li_2B_{10}H_{10}$. From the Pauling rules for ionic compounds, the coordination of metals can be estimated from the ratio of ionic radii of anions and cations.[39] This is particularly well observed in metal hydridoborates, where one can assume $B_{10}H_{10}^{2-}$ radii of 6.0 Å (5.8 Å for $B_{12}H_{12}^{2-}$). The size of the alkali metal cations increases with atomic number and according to Shannon radii is[40] 1.2 Å for Li, 1.9 Å for Na, 2.66 Å for K, 2.96 Å for Rb, and 3.38 Å for Cs. The ionic size ratio for compounds with $B_{10}H_{10}^{2-}$ anions is 0.20 for Li (3), 0.32 for Na (4), 0.44 for K (6), 0.49 for Rb (6), and 0.56 for Cs (6); numbers in parentheses indicate coordination numbers for anions. For compounds with $B_{12}H_{12}^{2-}$ anions, the formal coordination numbers are the same. In fact for all of these compounds, the cations are located within coordination tetrahedra between the nearest anions, as even for heavier alkali metals the ratio is close to 0.414, which is the limit of tetrahedral coordination. The structure analysis indicates that in the $P2_1/c$ structure of $(K,Rb,Cs)_2B_{10}H_{10}$ half of the cations are located at octahedral voids. The exceptions are Li and Na, where each cation is surrounded by three anions and thus is located at the face of coordination tetrahedra. The relation between the coordination number and lattice type is known to correlate with ionic conductivity,[31,41] and *bcc* anion packing is the ultimate for the best ion conductor.

In Figure 7, we present coordination polyhedra for $B_{10}H_{10}$ anions with Li and Na. Such a presentation reveals highly symmetric polyhedra for Li and Na. The positions of cations follow the *D*4*d* symmetry of the anion, forming a deformed cubic coordination for $Na_2B_{10}H_{10}$, and six Li cations surround the anion in $Li_2B_{10}H_{10}$. Among the symmetry elements of the *D*4*d* point group of the capped square antiprism that is $B_{10}H_{10}$, only those related to rotations are accessible due to thermal excitations (see Figure 7). Improper rotation by 45° (S_8) without reflection is the less energy demanding process that preserves the orientation of anions in the crystal opening additional sites for cations. This process will not change the hexagonal symmetry of the low-temperature phase. Rotation around one of the C_2 axes by 90° changes the orientation of the anion in the crystal lattice and thus breaks the *a,b,a,b* stacking of the *hcp* lattice. This is in fact observed in the high-temperature *ccp* structure of this compound, where the anions are still aligned along principal lattice directions with cations distributed in the tetrahedral void with similar Li−H separations as in the LT phase. The strong Li−H interaction in $Li_2B_{10}H_{10}$ is also related to low thermal expansion of this compound within the H-*c*-B class (see Table 2). As shown in Figure 6c for any configuration considered in the cubic phase, the shortest distance between hydrogen and lithium does not increase above 2.1 Å, which is consistent with the fact that with an increasing separation between anions the compounds disintegrate into molecular entities consisting of cations and anions.

The phase transition of $Na_2B_{10}H_{10}$ from the low-temperature $P2_1/c$ structure to the cubic $Fm\bar{3}m$ one is related to the orientational disorder of anions, while eight Na^+ ions effectively form regular cubic coordination around an anion (Figure 7). This is related to disorder in the cationic sublattice but not to changes in the anion coordination number.

CONCLUSION

In this work, a class of compounds, hydrido-*closo*-borates, has been structurally investigated using *in situ* X-ray diffraction methods under external pressure and temperature stimuli, combined with DFT calculations. Those materials have demonstrated very high compressibility and very low shear moduli, revealing highly malleable materials that would allow fast structural reconstruction under mechanical stresses. Furthermore, this family of compounds has exhibited very high CTEs, 2 orders of magnitude higher than those of oxides. Interestingly, our investigations reveal two new crystal phases, the first one for $K_2B_{12}H_{12}$ resulting from the pressure-induced phase transition around 2 GPa toward *Pnnm* symmetry and the second phase for which the transition is induced by temperature and transforms $Li_2B_{10}H_{10}$ from $P6_422$ to $Pa\bar{3}$ symmetry as suggested by DFT calculations. This study allows us to acquire a complete understanding of the crystal chemistry of this astonishing class of compounds and further confirms their trend for the *ccp* underlying anion packing.

https://doi.org/10.1021/acs.inorgchem.1c03681
Inorg. Chem. 2022, 61, 5224−5233

EXPERIMENTAL SECTION

Powder X-ray Diffraction. Samples were purchased from Katchem Co. The sample was measured at Swiss-Norwegian Beamline BM01 of the European Synchrotron Radiation Facility in Grenoble, France. A two-dimensional (2D) image plate detector (Pilatus 2M) positioned 411 mm from the sample was used with a wavelength of 0.71414 Å. The 2D diffraction patterns were integrated with Bubble software.[42] The sample detector geometry was calibrated with a LaB_6 NIST standard. For high-pressure experiments, the Diamond Anvil Cell (DAC), with a flat culet with a diameter of 600 μm, was loaded in an argon-filled glovebox (MBraun, <0.1 ppm O_2, <0.1 ppm H_2O). The samples were loaded with ruby crystals, for pressure calibration, into a 250 μm hole drilled in a stainless-steel gasket. No pressure-transmitting medium was used because of the low bulk modulus of these families of materials. For high-temperature experiments, the samples were loaded in a 0.5 mm glass capillary in the glovebox. The temperature was controlled using a Cyberstar hot blower. For hp-β-$K_2B_{12}H_{12}$ and ht-β-$Li_2B_{10}H_{10}$, the structures were determined using the isostructural models of hp3-ζ-$Na_2B_{12}H_{12}$ and rt-α-$Li_2B_{12}H_{12}$. The cell parameters were manually adjusted prior to their refinement using the Pawley algorithm implemented in TOPAS;[43] this algorithm was used also for the refinement of the cell parameters as a function of temperature and pressure. The refinements of the structure were performed using the Rietveld method,[44] in TOPAS.[43] For the hp polymorph, a spherical harmonic approach was used to simulate the strong preferential orientation caused by the DAC. The cell parameters as a function of temperature and pressure were refined using the Pawley algorithm.

DFT Calculations. Calculations were performed within DFT with a periodic plane wave basis set as implemented in Vienna ab initio Simulation Package.[45,46] The following calculation parameters were used: cutoff energy for basis set expansion of 700 eV, k-point sampling density (ka) of $\geq$20, convergence criterion for the electronic degrees of freedom of 10^{-6} eV/A, and for the structural relaxations the conjugated gradient method with a convergence of 10^{-2} eV/A. Projector-augmented wave potentials (PAW)[47,48] were used for atoms with electronic configurations of $1s^1$ for H, $2s^22p^1$ for B, $1s^22s^1$ for Li, $2p^63s^1$ for Na, $3p^64s^1$ for K, $4p^65s^1$ for Rb, and $5p^66s^1$ for Cs. The gradient-corrected (GGA) exchange-correlation functional and the nonlocal corrections accounting for a weak dispersive interactions were applied.[49−51] The normal modes at the Γ point were calculated in real space with atomic displacements of $\pm$0.1 Å in all symmetry inequivalent directions and visualized by placing Lorentzians with a half-width of 5 cm^{-1} for each mode. The normal mode frequencies were obtained by direct diagonalization of the dynamical matrix obtained from the forces calculated for displaced configurations. Elastic constants were calculated via deformation of the unit cell, $\pm$1% in each relevant direction and angle. For normal mode and elastic properties, fully optimized structures were used.

ASSOCIATED CONTENT

Supporting Information

The Supporting Information is available free of charge at https://pubs.acs.org/doi/10.1021/acs.inorgchem.1c03681.

> Calculation procedure for ht-$Li_2B_{10}H_{10}$, the result of the Rietveld refinement, the free energy as a function of the pressure and the transformation of the structures from *Pnnm* to $P2_1/c$ for hp-$K_2B_{12}H_{12}$ (Figures S1−S4), evolution of the cell volume as a function of pressure (Figure S5), and orientation of $B_{10}H_{10}^{2-}$ anions of ht-$Li_2B_{10}H_{10}$ with $Fm\bar{3}m$ and $Pa\bar{3}$ space groups (Figure S6) (PDF)

Accession Codes

CCDC 2123207 and 2123209 contain the supplementary crystallographic data for this paper. These data can be obtained free of charge via www.ccdc.cam.ac.uk/data_request/cif, or by emailing data_request@ccdc.cam.ac.uk, or by contacting The Cambridge Crystallographic Data Centre, 12 Union Road, Cambridge CB2 1EZ, UK; fax: +44 1223 336033.

AUTHOR INFORMATION

Corresponding Authors

Romain Moury − *Department of Physical Chemistry, University of Geneva, Geneva 1211, Switzerland; Institut des Molécules et Matériaux du Mans, University of le Mans, Le Mans 72085, France;* orcid.org/0000-0002-1198-2586; Email: romain.moury@univ-lemans.fr

Zbigniew Łodziana − *Institute of Nuclear Physics, Polish Academy of Sciences, Kraków 31342, Poland;* orcid.org/0000-0002-4713-6891; Email: Zbigniew.Lodziana@ifj.edu.pl

Hans Hagemann − *Department of Physical Chemistry, University of Geneva, Geneva 1211, Switzerland;* orcid.org/0000-0002-7183-8543; Email: Hans-Rudolf.Hagemann@unige.ch

Authors

Arndt Remhof − *Empa, Swiss Federal Laboratories for Materials Science and Technology, Dübendorf 8600, Switzerland;* orcid.org/0000-0002-8394-9646

Léo Duchêne − *Department of Physical Chemistry, University of Geneva, Geneva 1211, Switzerland; Empa, Swiss Federal Laboratories for Materials Science and Technology, Dübendorf 8600, Switzerland;* orcid.org/0000-0003-0309-4682

Elsa Roedern − *Empa, Swiss Federal Laboratories for Materials Science and Technology, Dübendorf 8600, Switzerland*

Angelina Gigante − *Department of Physical Chemistry, University of Geneva, Geneva 1211, Switzerland; Empa, Swiss Federal Laboratories for Materials Science and Technology, Dübendorf 8600, Switzerland;* orcid.org/0000-0002-7226-1360

Complete contact information is available at: https://pubs.acs.org/10.1021/acs.inorgchem.1c03681

Notes

The authors declare no competing financial interest.

ACKNOWLEDGMENTS

The authors thank V. Dmitriev, I. Dovgaliuk, and D. Chernyshov of the SNBL at ESRF for their support with the high-pressure experiments. The authors are thankful for the financial support from SNSF Sinergia Project CRSII2_160749 and SNSF Project 200021_169033/1. Z.Ł. acknowledges NCN support through Project 2019/01/Y/ST5/00046, 2015/17/B/ST3/02478 for elastic constants calculations, and CPU allocation at PL-Grid infrastructure.

REFERENCES

(1) Udovic, T. J.; Matsuo, M.; Unemoto, A.; Verdal, N.; Stavila, V.; Skripov, A. V.; Rush, J. J.; Takamura, H.; Orimo, S. I. Sodium Superionic Conduction in $Na_2B_{12}H_{12}$. *Chem. Commun.* **2014**, *50* (28), 3750−3752.

(2) Hansen, B. R. S. S.; Paskevicius, M.; Li, H.-W. W.; Akiba, E.; Jensen, T. R. Metal Boranes: Progress and Applications. *Coord. Chem. Rev.* **2016**, *323*, 60−70.

(3) Duchêne, L.; Remhof, A.; Hagemann, H.; Battaglia, C. Status and Prospects of Hydroborate Electrolytes for All-Solid-State Batteries. *Energy Storage Mater.* **2020**, *25*, 782−794.
(4) Brighi, M.; Murgia, F.; Černý, R. Closo-Hydroborate Sodium Salts as an Emerging Class of Room-Temperature Solid Electrolytes. *Cell Reports Phys. Sci.* **2020**, *1* (10), 100217.
(5) Kim, S.; Oguchi, H.; Toyama, N.; Sato, T.; Takagi, S.; Otomo, T.; Arunkumar, D.; Kuwata, N.; Kawamura, J.; Orimo, S. ichi. A Complex Hydride Lithium Superionic Conductor for High-Energy-Density All-Solid-State Lithium Metal Batteries. *Nat. Commun.* **2019**, *10*, 1081.
(6) Brighi, M.; Murgia, F.; Łodziana, Z.; Schouwink, P.; Wołczyk, A.; Černý, R. A Mixed Anion Hydroborate/Carba-Hydroborate as a Room Temperature Na-Ion Solid Electrolyte. *J. Power Sources* **2018**, *404*, 7−12.
(7) Tang, W. S.; Yoshida, K.; Soloninin, A. V.; Skoryunov, R. V.; Babanova, O. A.; Skripov, A. V.; Dimitrievska, M.; Stavila, V.; Orimo, S.; Udovic, T. J. Stabilizing Superionic-Conducting Structures via Mixed-Anion Solid Solutions of Monocarba- Closo -Borate Salts. *ACS Energy Lett.* **2016**, *1* (4), 659−664.
(8) Tang, W. S.; Matsuo, M.; Wu, H.; Stavila, V.; Zhou, W.; Talin, A. A.; Soloninin, A. V.; Skoryunov, R. V.; Babanova, O. A.; Skripov, A. V.; Unemoto, A.; Orimo, S.-I.; Udovic, T. J. Liquid-Like Ionic Conduction in Solid Lithium and Sodium Monocarba-Closo-Decaborates Near or at Room Temperature. *Adv. Energy Mater.* **2016**, *6* (8), 1502237.
(9) Payandeh, S. H.; Rentsch, D.; Łodziana, Z.; Asakura, R.; Bigler, L.; Černý, R.; Battaglia, C.; Remhof, A. Nido-Hydroborate-Based Electrolytes for All-Solid-State Lithium Batteries. *Adv. Funct. Mater.* **2021**, *31* (18), 2010046.
(10) Payandeh, S.; Asakura, R.; Avramidou, P.; Rentsch, D.; Łodziana, Z.; Černý, R.; Remhof, A.; Battaglia, C. Nido-Borate/Closo-Borate Mixed-Anion Electrolytes for All-Solid-State Batteries. *Chem. Mater.* **2020**, *32* (3), 1101−1110.
(11) Fisher, S. P.; Tomich, A. W.; Lovera, S. O.; Kleinsasser, J. F.; Guo, J.; Asay, M. J.; Nelson, H. M.; Lavallo, V. Nonclassical Applications of Closo-Carborane Anions: From Main Group Chemistry and Catalysis to Energy Storage. *Chem. Rev.* **2019**, *119* (14), 8262−8290.
(12) Jørgensen, M.; Shea, P. T.; Tomich, A. W.; Varley, J. B.; Bercx, M.; Lovera, S.; Černý, R.; Zhou, W.; Udovic, T. J.; Lavallo, V.; Jensen, T. R.; Wood, B. C.; Stavila, V. Understanding Superionic Conductivity in Lithium and Sodium Salts of Weakly Coordinating Closo-Hexahalocarbaborate Anions. *Chem. Mater.* **2020**, *32* (4), 1475−1487.
(13) Muetterties, E. L.; Balthis, J. H.; Chia, Y. T.; Knoth, W. H.; Miller, H. C. Chemistry of Boranes. VIII. Salts and Acids of $B_{10}H_{10}^{-2}$ and $B_{12}H_{12}^{-2}$. *Inorg. Chem.* **1964**, *3* (3), 444−451.
(14) Asakura, R.; Duchêne, L.; Kühnel, R. S.; Remhof, A.; Hagemann, H.; Battaglia, C. Electrochemical Oxidative Stability of Hydroborate-Based Solid-State Electrolytes. *ACS Appl. Energy Mater.* **2019**, *2* (9), 6924−6930.
(15) Duchêne, L.; Kühnel, R.-S.; Stilp, E.; Cuervo Reyes, E.; Remhof, A.; Hagemann, H.; Battaglia, C. A Stable 3 V All-Solid-State Sodium−Ion Battery Based on a Closo -Borate Electrolyte. *Energy Environ. Sci.* **2017**, *10* (12), 2609−2615.
(16) Murgia, F.; Brighi, M.; Černý, R. Room-Temperature-Operating Na Solid-State Battery with Complex Hydride as Electrolyte. *Electrochem. commun.* **2019**, *106*, 106534.
(17) Moury, R.; Gigante, A.; Hagemann, H. An Alternative Approach to the Synthesis of NaB_3H_8 and $Na_2B_{12}H_{12}$ for Solid Electrolyte Applications. *Int. J. Hydrogen Energy* **2017**, *42*, 22417−22421.
(18) Gigante, A.; Duchêne, L.; Moury, R.; Pupier, M.; Remhof, A.; Hagemann, H. Direct Solution-Based Synthesis of $Na_4(B_{12}H_{12})$-$(B_{10}H_{10})$ Solid Electrolyte. *ChemSusChem* **2019**, *12* (21), 4832−4837.
(19) Duchêne, L.; Kim, D. H.; Song, Y. B.; Jun, S.; Moury, R.; Remhof, A.; Hagemann, H.; Jung, Y. S.; Battaglia, C. Crystallization of Closo-Borate Electrolytes from Solution Enabling Infiltration into Slurry-Casted Porous Electrodes for All-Solid-State Batteries. *Energy Storage Mater.* **2020**, *26*, 543.
(20) Brighi, M.; Murgia, F.; Černý, R. Mechanical Behavior and Dendrite Resistance of Closo-Hydroborate Solid Electrolyte. *Adv. Mater. Interfaces* **2022**, *9*, 2101254.
(21) Asakura, R.; Reber, D.; Duchêne, L.; Payandeh, S.; Remhof, A.; Hagemann, H.; Battaglia, C. 4 V Room-Temperature All-Solid-State Sodium Battery Enabled by a Passivating Cathode/Hydroborate Solid Electrolyte Interface. *Energy Environ. Sci.* **2020**, *13* (12), 5048−5058.
(22) Frenck, L.; Sethi, G. K.; Maslyn, J. A.; Balsara, N. P. Factors That Control the Formation of Dendrites and Other Morphologies on Lithium Metal Anodes. *Frontiers in Energy Research* **2019**, *7*, 115.
(23) Sau, K.; Ikeshoji, T.; Takagi, S.; Orimo, S.-i.; Errandonea, D.; Chu, D.; Cazorla, C. Colossal Barocaloric Effects in the Complex Hydride Li2B12H12. *Sci. Rep.* **2021**, *11* (1), 11915.
(24) Černý, R.; Brighi, M.; Murgia, F. The Crystal Chemistry of Inorganic Hydroborates. *Chemistry* **2020**, *2* (4), 805−826.
(25) Wu, H.; Tang, W. S.; Stavila, V.; Zhou, W.; Rush, J. J.; Udovic, T. J. Structural Behavior of Li2B10H10. *J. Phys. Chem. C* **2015**, *119* (12), 6481−6487.
(26) Verdal, N.; Wu, H.; Udovic, T. J.; Stavila, V.; Zhou, W.; Rush, J. J. Evidence of a Transition to Reorientational Disorder in the Cubic Alkali-Metal Dodecahydro-Closo-Dodecaborates. *J. Solid State Chem.* **2011**, *184* (11), 3110−3116.
(27) Moury, R.; Łodziana, Z.; Remhof, A.; Duchêne, L.; Roedern, E.; Gigante, A.; Hagemann, H. Pressure-Induced Phase Transitions in $Na_2B_{12}H_{12}$, Structural Investigation on a Candidate for Solid- State Electrolyte. *Acta Crystallogr., Sect. B: Struct. Sci., Cryst. Eng. Mater.* **2019**, *75* (3), 406−413.
(28) Benham, V.; Lord, G.; Butler, I. S.; Gilson, D. F. R. High-Pressure Diamond-Anvil-Cell Micro-Raman Spectra of Mercuric Cyanide, $Hg(CN)_2$, and Cesium Dodecahydroborate, $Cs_2[B_{12}H_{12}]$: *Appl. Spectorscopy* **1987**, *41* (5), 915−917.
(29) Paskevicius, M.; Pitt, M. P.; Brown, D. H.; Sheppard, D. A.; Chumphongphan, S.; Buckley, C. E. First-Order Phase Transition in the $Li_2B_{12}H_{12}$ System. *Phys. Chem. Chem. Phys.* **2013**, *15* (38), 15825−15828.
(30) Verdal, N.; Her, J. H.; Stavila, V.; Soloninin, A. V.; Babanova, O. A.; Skripov, A. V.; Udovic, T. J.; Rush, J. J. Complex High-Temperature Phase Transitions in $Li_2B_{12}H_{12}$ and $Na_2B_{12}H_{12}$. *J. Solid State Chem.* **2014**, *212*, 81−91.
(31) Wang, Y.; Richards, W. D.; Ong, S. P.; Miara, L. J.; Kim, J. C.; Mo, Y.; Ceder, G. Design Principles for Solid-State Lithium Superionic Conductors. *Nat. Mater.* **2015**, *14* (10), 1026−1031.
(32) Schranz, W.; Tröster, A.; Koppensteiner, J.; Miletich, R. Finite Strain Landau Theory of High Pressure Phase Transformations. *J. Phys.: Condens. Matter* **2007**, *19* (27), 275202.
(33) Orobengoa, D.; Capillas, C.; Aroyo, M. I.; Perez-Mato, J. M. AMPLIMODES: Symmetry-Mode Analysis on the Bilbao Crystallographic Server. *J. Appl. Crystallogr.* **2009**, *42* (5), 820−833.
(34) Perez-Mato, J. M.; Orobengoa, D.; Aroyo, M. I. Mode Crystallography of Distorted Structures. *Acta Crystallogr., Sect. A: Found. Adv.* **2010**, *66* (5), 558−590.
(35) Wang, Z. Q.; Wu, M. S.; Liu, G.; Lei, X. L.; Xu, B.; Ouyang, C. Y. Elastic Properties of New Solid State Electrolyte Material $Li_{10}GeP_2S_{12}$: A Study from First-Principles Calculations. *Int. J. Electrochem. Sci.* **2014**, *9*, 562−568.
(36) Pugh, S. F. XCII. Relations between the Elastic Moduli and the Plastic Properties of Polycrystalline Pure Metals. *London, Edinburgh, Dublin Philos. Mag. J. Sci.* **1954**, *45* (367), 823−843.
(37) Sethio, D.; Lawson Daku, L. M.; Hagemann, H. A Theoretical Study of the Spectroscopic Properties of B_2H_6 and of a Series of $B_xH_y^{z-}$ Species (x = 1−12, y = 3−14, z = 0−2): From BH_3 to $B_{12}H_{12}^{2-}$. *Int. J. Hydrogen Energy* **2016**, *41* (16), 6814−6824.
(38) Hagemann, H.; Sharma, M.; Sethio, D.; Lawson Daku, L. M. Correlating Boron−Hydrogen Stretching Frequencies with Boron−Hydrogen Bond Lengths in Closoboranes: An Approach Using DFT Calculations. *Helv. Chim. Acta* **2018**, *101* (2), e1700239.

https://doi.org/10.1021/acs.inorgchem.1c03681
Inorg. Chem. 2022, 61, 5224−5233

(39) Pauling, L. The Principles Determining the Structure of Complex Ionic Crystals. *J. Am. Chem. Soc.* **1929**, *51* (4), 1010−1026.
(40) Shannon, R. D.; IUCr.. Revised Effective Ionic Radii and Systematic Studies of Interatomic Distances in Halides and Chalcogenides. *Acta Crystallogr., Sect. A* **1976**, *32* (5), 751−767.
(41) Sadikin, Y.; Schouwink, P.; Brighi, M.; Łodziana, Z.; Černý, R. Modified Anion Packing of $Na_2B_{12}H_{12}$ in Close to Room Temperature Superionic Conductors. *Inorg. Chem.* **2017**, *56* (9), 5006−5016.
(42) Dyadkin, V.; Pattison, P.; Dmitriev, V.; Chernyshov, D. A New Multipurpose Diffractometer PILATUS@SNBL. *J. Synchrotron Radiat.* **2016**, *23* (3), 825−829.
(43) Coelho, A. A. Whole-Profile Structure Solution from Powder Diffraction Data Using Simulated Annealing. *J. Appl. Crystallogr.* **2000**, *33* (3), 899−908.
(44) Rietveld, H. M. A Profile Refinement Method for Nuclear and Magnetic Structures. *J. Appl. Crystallogr.* **1969**, *2* (2), 65−71.
(45) Kresse, G.; Furthmüller, J. Efficient Iterative Schemes for *Ab Initio* Total-Energy Calculations Using a Plane-Wave Basis Set. *Phys. Rev. B* **1996**, *54* (16), 11169.
(46) Kresse, G.; Furthmüller, J. Efficiency of Ab-Initio Total Energy Calculations for Metals and Semiconductors Using a Plane-Wave Basis Set. *Comput. Mater. Sci.* **1996**, *6* (1), 15−50.
(47) Blöchl, P. E. Projector Augmented-Wave Method. *Phys. Rev. B* **1994**, *50* (24), 17953.
(48) Kresse, G.; Joubert, D. From Ultrasoft Pseudopotentials to the Projector Augmented-Wave Method. *Phys. Rev. B* **1999**, *59* (3), 1758.
(49) Perdew, J. P.; Burke, K.; Ernzerhof, M. Generalized Gradient Approximation Made Simple. *Phys. Rev. Lett.* **1996**, *77* (18), 3865.
(50) Dion, M.; Rydberg, H.; Schröder, E.; Langreth, D. C.; Lundqvist, B. I. Van Der Waals Density Functional for General Geometries. *Phys. Rev. Lett.* **2004**, *92* (24), 246401.
(51) Maniadaki, A. E.; Łodziana, Z. Theoretical Description of Alkali Metal Closo-Boranes − towards the Crystal Structure of $MgB_{12}H_{12}$. *Phys. Chem. Chem. Phys.* **2018**, *20* (48), 30140−30149.

https://doi.org/10.1021/acs.inorgchem.1c03681
Inorg. Chem. 2022, 61, 5224−5233